A time-lapse imaging platform for quantification of soil crack development due to simulated root water uptake

Tino Colombi[a,*], Norbert Kirchgessner[b], Daniel Iseskog[a], Susanne Alexandersson[a], Mats Larsbo[a], Thomas Keller[a,c]

[a] *Department of Soil and Environment, Swedish University of Agricultural Sciences (SLU), Box 7014, SE-75007, Uppsala, Sweden*
[b] *Institute of Agricultural Sciences, ETH Zurich, Universitätstrasse 2, CH-8092, Zurich, Switzerland*
[c] *Department of Agroecology and Environment, Agroscope, Reckenholzstrasse 191, CH-8046, Zürich, Switzerland*

ABSTRACT

Plants are major drivers of soil structure dynamics. Root growth creates new macropores and provides essential carbon to soil, while root water uptake may induce crack formation around roots. Cracks can facilitate root growth as they provide pathways of least resistance and improve water infiltration and soil aeration. Due to the lack of suitable quantification methods, knowledge on the effects of root water uptake on soil crack formation remains limited. In the current study, we developed a time-lapse imaging platform that allows i) simulating root water uptake through localized soil drying and ii) quantifying the development of two-dimensional crack networks. Customized soil boxes that were 50 mm wide, 55 mm high and 5 mm deep were designed. Artificial roots made of dialysis tubes were inserted into the soil boxes and polyethylene glycol solution was circulated through the tubes. This induced a gradient in osmotic potential at the contact area (150 mm^2) between the soil and the dialysis tubes, resulting in controlled soil drying. Drying intensity was varied by using different polyethylene glycol concentrations. Experiments were conducted with three soils that were subjected to three drying intensities for 6.5 days. We developed a time-lapse imaging system to record soil crack formation at two-minute intervals in twelve samples simultaneously. Resulting crack networks were quantified with an automated image analysis pipeline. Across soils and drying intensities, crack network development slowed down after 24–48 h of soil drying. The extent and complexity of crack networks increased with drying intensity and crack networks were larger and more complex in the clay and clay loam soil than in the silt loam soil. Smaller and less complex crack networks were better connected than larger and more complex networks. These results demonstrate that the platform developed in this study is suitable to quantify crack network development in soil due to simulated root water uptake at high temporal resolution and high throughput. Thereby, it can provide information needed to improve our understanding on how plants modify soil structure.

1. Introduction

Soil structure, referring to the spatial arrangement of solids and pores, is crucial for the functioning of terrestrial ecosystems. It forms the living space for soil organisms, controls transport of fluids and particles and contributes to soil physical stability (Angers and Caron, 1998; Bronick and Lal, 2005; Jarvis, 2007; Jin et al., 2013; Lavelle et al., 1997; Rabot et al., 2018; Young et al., 1998). Hence, biogeochemical cycles, soil biodiversity, water regulation and purification, leaching and runoff of nutrients, and last but not least agricultural production are all highly dependent on soil structure (Ghezzehei, 2012;

Rabot et al., 2018; Vogel et al., 2018; Young et al., 1998). The structure of arable soils undergoes constant modification due to anthropogenic intervention such as tillage and field traffic, and due to natural processes including both abiotic and biotic phenomena (Bronick and Lal, 2005; Dexter, 1991; Hamza and Anderson, 2005; Rabot et al., 2018).

Plants are essential for all soil biological processes that are involved in soil structure dynamics (Colombi and Keller, 2019). Organic matter inputs to soil through plant litter form the fundamental energy source for heterotrophic soil organisms. In turn, heterotrophic soil life including micro-, meso- and macro-organisms modifies soil structure through excretion of various extracellular substances, enmeshment of
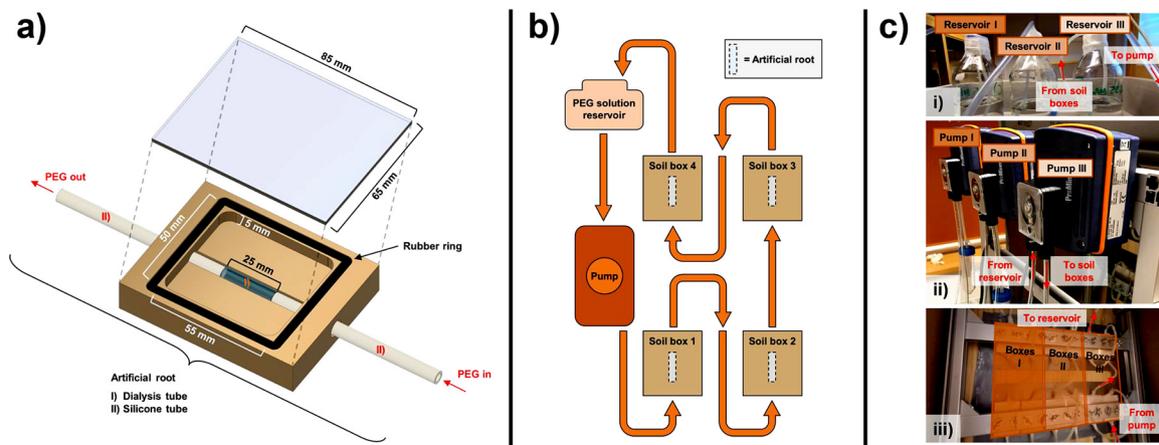
Fig. 1. Different components used to induce localized soil drying: a) Soil boxes with artificial roots through which polyethylene (PEG) solution was pumped to create an osmotic potential difference at the contact area between dialysis tube and the soil. b) Schematic representation of the drying system in which PEG solution was pumped from reservoir through four samples in series before being returned to the reservoir. c) Pictures of the drying system with i) PEG solution reservoirs, ii) peristaltic pumps, and iii) soil boxes.

soil particles, and soil bioturbation (Capowiez et al., 2012; Cheik et al., 2019; Hallett et al., 2013; Kautz et al., 2014; Lavelle et al., 1997; Oades, 1993). The role of plants for soil structure dynamics is however not restricted to the input of organic matter. Root exudation and particle enmeshment by roots contribute to soil structure stabilization and de-stabilization (Bronick and Lal, 2005; Hallett et al., 2013; Oades, 1993), while root growth displaces soil particles and creates new soil macropores (Koestel and Schlüter, 2019; Lucas et al., 2019a; Pulido-Moncada et al., 2020; Tracy et al., 2012). Moreover, root water uptake contributes to soil structure dynamics (Materechera et al., 1992). Transpiration, which is regulated by the opening and closing of stomata, induces water flow from the soil into the roots. As a result, soil surrounding the roots dries out. Such localized soil drying can cause soil shrinkage, which eventually leads to crack formation around roots. Soil macropores such as cracks and biopores provide pathways of least resistance and improve water infiltration and soil aeration, which in turn can increase plant growth (Atkinson et al., 2020; Colombi et al., 2017; Stirzaker et al., 1996; Zhang et al., 2014). Due to their broad implications for soil structure dynamics, plants are suggested to play a key role in the maintenance of soil structure as well as in the amelioration of structurally degraded soils (Colombi and Keller, 2019; Dexter, 1991; Hamza and Anderson, 2005).

The advent of digital imaging techniques such as X-ray and neutron imagining in soil science has offered new possibilities to study soil structure dynamics (Tracy et al., 2011). Several recent studies quantified effects of root growth on soil structure development in remoulded soil and undisturbed soil samples taken from the field using X-ray tomography (Koestel and Schlüter, 2019; Lucas et al., 2019b, 2019a; Pulido-Moncada et al., 2020; Tracy et al., 2012). Neutron imaging allows measuring root water uptake in situ (Mawodza et al., 2020; Tötzke et al., 2017; Zarebanadkouki et al., 2014). However, the understanding of the effects of root water uptake on soil structure dynamics remains limited. X-ray and neutron imaging have the advantage that processes can be quantified in three dimensions but their temporal resolution is limited due to time-consuming image acquisition and analysis. Furthermore, both methods are costly, which often limits sample throughput and thus the number of specimens that can be investigated. Automated time-lapse imaging using RGB cameras is a viable alternative that can overcome these limitations as shown in previous studies that applied time-lapse imaging to quantify crack patterns due to evaporative drying (Decarlo and Shokri, 2014; Tran et al., 2019; Zhang et al., 2020; Zhu et al., 2020).

The variable nature of plants further complicates quantification of soil structure dynamics due to root water uptake. On the one hand,

water uptake is not uniform across the root system and gradients in water uptake may occur even along a single root (Zarebanadkouki et al., 2014, 2013). Hence, it is difficult to localize exactly where root water uptake takes place. On the other hand, root water potential differs between plant species, between individual plants of the same species, and among individual roots of a single plant (Crombie et al., 1988; Simonneau et al., 1998; Williams, 1976). Moreover, environmental stresses such as low soil moisture can influence root water potential (Fiscus, 1972; Sharp and Davies, 1979; Zwieniecki and Boersma, 1997). Therefore, approaches that allow control of the location and intensity of water uptake are needed to investigate the effects of root water uptake on soil structure dynamics. Such approaches can be then combined with methods that enable to quantify the development of soil crack networks at high temporal resolution and high throughput.

The aims of the current study were i) to develop a platform that allows quantifying crack network development in soil due to simulated root water uptake and ii) to test this platform using three soils and three different water potentials. To simulate root water uptake, soil samples were subjected to 6.5 days of localized drying using polyethylene glycol solution. Automated time-lapse imaging was deployed to record crack network development in two-minute intervals. Finally, we developed an image analysis pipeline to quantify parameters describing the development of the extent, the complexity and the connectivity of the crack network.

2. Material and methods

2.1. Design of soil boxes and artificial roots for localized soil drying

Experiments were conducted in small customized soil boxes (Fig. 1a), which were manufactured from Polylactide (PLA) plastic (Add North 3D AB, Ölsremma, Sweden) using a benchtop 3D printer (Ultimaker 3 Extended, Ultimaker, Utrecht, Netherlands). The inner compartment of the boxes was 5 mm deep, 50 mm wide and 55 mm high, and the edges were rounded with a 5 mm radius. Soil was filled into the boxes through the open front side. For the experiments, the front side was closed with a 2 mm thick Plexiglas cover so that the entire surface of the sample was visible. A rubber ring was placed between the soil box and the Plexiglas cover to avoid contact between the soil sample and the cover (Fig. 1a).

Artificial roots were designed to induce and control localized soil drying, mimicking root water uptake. They were made of semi-permeable dialysis tubes with a 14'000 molecular weight cut-off (Dialysis tubing cellulose membrane, Sigma Aldrich, St. Louis, MO,

Table 1
Basic physiochemical properties of soils used in the study. All soils were taken from the topsoil (0-25 cm) of arable fields around Uppsala, Sweden.

	Clay	Clay loam	Silt loam
Coordinates	59.82 °N; 17.65 °E	59.81 °N; 17.65 °E	59.83 °N; 17.71 °E
Clay/Silt/Sand [%]	42.1/31.4/26.5	38.9/34.5/26.5	21.5/52.8/25.8
SOM [g 100 g^{-1}]	0.6	0.9	3.5
pH (H_2O)	6.0	5.6	6.9
$\rho_{b, initial}$ [g cm^{-3}]	1.3	1.3	1.3
ρ_p [g cm^{-3}]	2.65	2.66	2.56
ε [cm^3 cm^{-3}]	0.51	0.51	0.49
$\theta_{initial}$ [cm^3 cm^{-3}]	0.41	0.41	0.39
$w_{initial}$ [g^3 g^{-3}]	0.31	0.31	0.30

Abbreviations: SOM = soil organic matter, $\rho_{b, initial}$ = initial bulk density, ρ_p = particle density, ε = total porosity, $\theta_{initial}$ = initial volumetric water content, $w_{initial}$ = initial gravimetric water content.

Table 2
Concentration of polyethylene glycol 20′000 (PEG) solution (ρ_i), osmolality (c) and osmotic potential (ψ) at low, moderate and high drying intensity.

Drying intensity	ρ_i [g PEG l^{-1} ddH_2O]	c [mol kg^{-1}]	ψ [MPa]
Low	155.1	0.143	−0.35
Moderate	199.2	0.294	−0.72
High	244.1	0.613	−1.50

United States). The dialysis tubes (25 mm long, 6 mm diameter) were connected tightly to silicone tubes on both ends. Artificial roots were placed into an open channel of 7 mm diameter at the backside of the boxes, which ran vertically through the centre of the box. Soil was packed on top of the channel, creating a contact area of approximately 150 mm^2 between the dialysis tube and the soil at the centre of the sample (Fig. 1a). A difference in osmotic potential at the contact area between the soil and the dialysis tube was induced by circulating polyethylene glycol (PEG, molecular weight: 20′000) solution through the artificial roots using peristaltic pumps (DULCO flex DF2a, ProMinent GmbH, Heidelberg, Germany) (Fig. 1b).

2.2. Soil properties and sample preparation

We used three different soils taken from the top 25 cm of arable fields around Uppsala, Sweden (Table 1). The different soils had clay contents of 21.5 %, 38.9 % and 42.1 % and were classified as silt loam, clay loam and clay soil, respectively (United States Department of Agriculture, 2020). Soil organic matter content was between 0.6 % and 3.5 % and pH (H_2O) varied from 5.6 to 6.9 (Table 1). Soils were air-dried to approximately 17 % gravimetric water content and plant and animal debris were removed manually. The soil was then passed through a sieve with 2 mm mesh width, homogenized and stored in bags at 4 °C to avoid water loss.

Sieved soil was filled into the soil boxes and homogenously packed to a height of 5 mm to a dry bulk density of 1.3 g cm^{-3}. Tap water was added to the sample during packing to achieve 80 % water saturation. Resulting gravimetric water contents were 0.31 g g^{-1} for the clay and clay loam soil and 0.30 g g^{-1} for the silt loam soil (Table 1). The visible surface of the soil was gently smeared with a razorblade to further homogenize the sample. Anti-fog spray (The Aquatic, Look Clear S.R.L., Lecco, Italy) helped to minimize condensation on the Plexiglas cover. To avoid evaporation from the soil sample, the cover was attached to the soil box with self-sealing parafilm. Samples were then left for 24 h at room temperature to reach equilibrium distribution of water in the sample.

2.3. Simulation of different root water potentials and experimental set-up

We used different concentrations of PEG solution to simulate different root water potentials. The osmolality of different concentrations (50, 100, 150, 200, 250 g PEG l^{-1} ddH_2O) was measured with an osmometer using the freezing point depression method (Advanced Instruments, 3250 Single-Sample Osmometer, Norwood, MA, USA). Following Money (1989), osmolality (c) was converted into osmotic potential (ψ) as:

$$\Psi[Mpa] = -2.446 kg\ MPa\ mol^{-1} * c[mol\ kg^{-1}] \tag{1}$$

A logarithmic regression model (R^2 = 0.99, Supplemental Figure

S1) was then used to determine the PEG solution concentration (g PEG l^{-1} ddH_2O) needed to achieve osmotic potentials of -0.35 MPa, -0.72 MPa and -1.50 MPa These values reflect a range of root water potentials reported for different plant species (Crombie et al., 1988; Fiscus, 1972; Sharp and Davies, 1979; Simonneau et al., 1998; Williams, 1976; Zwieniecki and Boersma, 1997) and simulated soil drying by roots at low (-0.35 MPa), moderate (-0.72 MPa), and high (-1.50 MPa) intensity (Table 2).

Solution was prepared in 1.5 L glass reservoirs using 1 L ddH_2O and the required amount of PEG. A peristaltic pump working at a rate of 1.44 L h^{-1} pumped solution from a reservoir through four individual soil boxes in series back into the reservoir bottle (Fig. 1b). This closed system enabled continuous circulation of PEG solution through the samples during the entire experiment. Samples were fixed in upright position to an aluminum frame. The set-up was equipped with three pumps. This allowed running experiments simultaneously in twelve samples allocated in two rows of six soil boxes each (Fig. 1c). Each drying experiment lasted 6.5 days, and each combination of soil type and drying intensity was replicated four times (n = 4).

2.4. Image acquisition

Crack development due to soil drying was recorded through automated time-lapse imaging in 2 min intervals. We used two mirror-less cameras (Canon EOS M6, Canon, Tokyo, Japan) with 24 megapixel sensors. The cameras were equipped with macro lenses (EF-M 28 mm f1/3 IS STM, Canon, Tokyo, Japan) and set to an aperture value of f/22, an exposure time of 1/6 s, and a film speed of 100 ISO. The distance between the lens and the surface of the soil sample was 120 mm, resulting in a pixel edge length of 16 μm.

To ensure constant illumination on the soil surface, a custom-made illumination system was fixed to the camera lens. The illumination system consisted of a pyramid-shaped hood that was manufactured using a 3D printer (Ultimaker 3 Extended) and white 12 V LED strips (RS PRO LS Series, White LED Strip 12 V, RS Components AB, Gothenburg, Sweden). The hood had an open square base with 96 mm edge length that faced the transparent front side of the soil boxes (Fig. 2a). LED strips were attached to all four edges at the open base of the hood to provide constant illumination. To minimize reflections on the Plexiglas cover, the light direction was perpendicular to the image plane. The distance between the open base of the hood and the image plane was 5 mm. The inside surfaces of the hood were covered with aluminium foil to further homogenise the illumination. The camera lens was inserted into the hood through a hole at the apex of the hood (Fig. 2a). To avoid influences from external light, the imaging system remained closed during experiments.

The two cameras with attached illumination hoods were fixed onto camera dollies. The dollies were attached to aluminium rails (Norcan, Haguenau Cedex, France) on which they could move back and forth (Fig. 2b). A rubber timing belt was fixed to each dolly and connected via a gearwheel to a stepper motor (Nema 17 Bipolar 1.8deg 45Ncm, Fulling Motor Co., Ltd., Changzhou, China). A motor driver (Adafruit Motor Shield V2, Adafruit Industries, New York City, NY, United States) in combination with an Arduino microcontroller (Arduino Mega 2560, Arduino AG, Somerville, MA, United States) allowed controlling the movement of the dolly. The same microcontroller was used to trigger
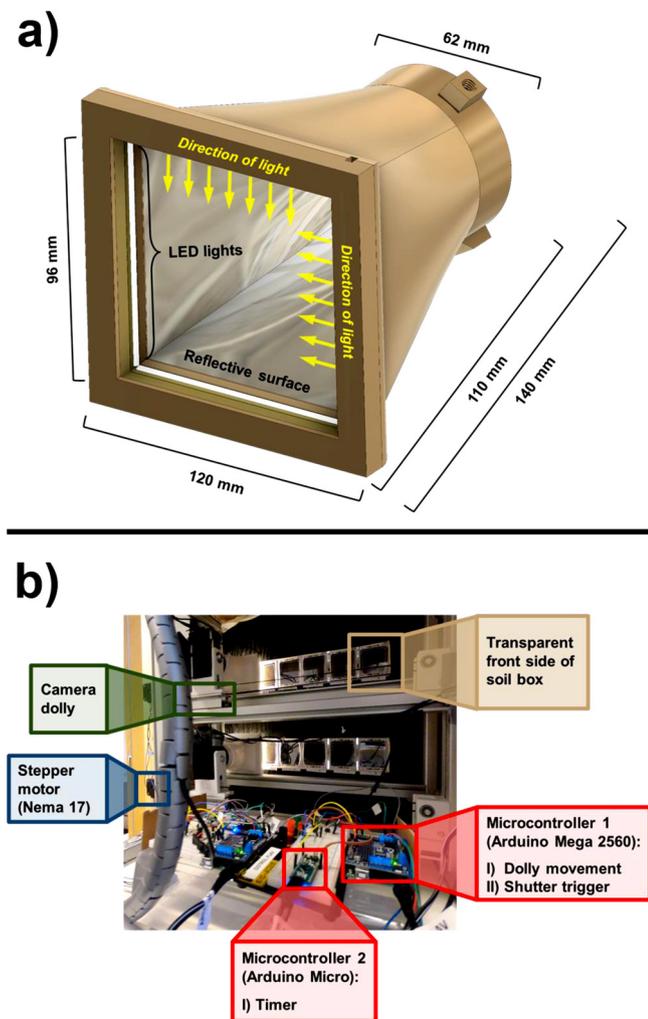
Fig. 2. Different components of the imaging system used to record crack development due to localized soil drying. a) Illustration of illumination hood fixed to the camera lens to ensure constant light conditions using white 12 V LED strips. b) Back view of the imaging system depicting (green) camera dollies, (blue) stepper motors, (red) Arduino microcontrollers controlling the movement of the dolly, triggering camera shutters, and controlling time-lapse intervals, and (brown) soil boxes allocated in two rows of six boxes each.

the camera shutter. To achieve constant time intervals between pictures taken from the same sample, a timer was implemented using another Arduino microcontroller (Arduino Micro). Codes for the microcontrollers were programmed in Arduino IDE version 1.8.9. Both cameras were connected to an independent control system and therefore operated independently (Fig. 2b). Unique QR codes were placed below each box to enable images to be automatically assigned to correct samples (Fig. 3). Four black round position markers were attached to the Plexiglass cover above and below the soil sample at a fixed horizontal distance of 42.5 mm to obtain pixel resolution. These markers were also used to correct for horizontal drift in the camera position caused by slight expansions of the timing belt and seldom inconsistencies of the stepper motors. Pictures were stored as. JPEG files (Fig. 3).

2.5. Image processing

Image processing was performed with a set of analysis scripts, which were all programmed in a Matlab 2018b environment (The Mathworks, Natick, MA, United States). To process the high number of acquired images (> 4500 images per sample), images analysis was almost

completely automatized and only required a minimum of manual intervention (< 2 min per sample).

First, images were sorted and prepared for quantitative analysis of the crack network. QR codes in the images were decoded (Shapira, 2015) and images taken from the same sample were allocated to a separate folder. The pixel resolution of the images was obtained from the black round position markers that were allocated around each soil sample and written to. EXIF tags (Harvey, 2018). Next, horizontal drift in the camera position among pictures from the same sample was corrected using the central coordinates of the position markers (Fig. 3). The adhesion between the soil and the wall of the box was weaker than the cohesion within the soil, which often resulted in gaps opening close to the walls during drying. To avoid those gaps in the analysis of crack networks, we chose a region of interest that was slightly smaller than the surface area of the soil sample, i.e. 40 mm wide and 45 mm high (Fig. 3).

Images were then converted from RGB to monochrome. Despite the implemented illumination system, there were still slight inhomogeneities in brightness across the region of interest caused by reflections on the Plexiglas. These inhomogeneities were quantified from pictures taken of soil boxes that were filled with white paper instead of soil and used to normalize the brightness of every image (Fig. 3). Pixels with a brightness lower than 0.6 were classified as cracks and were segmented from the soil. Regions classified as cracks that were smaller than 100 pixels were discarded and background patches smaller than 100 pixels were filled to avoid loops. Finally, region growing was performed (Kroon, 2009) in an eight pixel neighbourhood with a maximum difference in intensities of 0.1 using the previous segmentation and the normalized image, which resulted in the final crack mask (Fig. 3). This mask was skeletonized (Solís Montero and Lang, 2012) and a Euclidian distance map of the crack network was computed (Fig. 3). From this, metrics describing the extent, the connectivity, and the complexity of the crack network were obtained. Crack area, i.e. the number of pixels within the region of interest classified as crack, was used as a first descriptor of the extent of the crack network. Crack length and the distribution of crack widths across the crack network were obtained from the skeleton and the Euclidian distance map, respectively. These properties were used as further metrics associated with the extent of the crack network. The number of individual crack clusters, i.e. cracks that were not connected to each other, was used as a surrogate metric for the connectivity of the crack network. The complexity of the crack network was determined by the number of endpoints and the number of junctions within the crack skeleton. Data from every single image was saved as a separate. JSON file (Fig. 3).

2.6. Quantification of soil shrinkage and changes in soil water content

At the end of each experiment, i.e. after 6.5 days of soil drying, soil shrinkage and changes in soil water content were determined. Soil shrinkage was calculated as the proportion between total crack area and the area of the region of interest. Samples were weighed upon completion of the drying experiments, dried at 105 °C for 48 h, and weighed again to determine gravimetric water content.

2.7. Data analysis and statistics

Data processing, statistical analyses, and data visualization were carried out in R version 3.4.1 (R Core Team, 2017). Data obtained from Matlab scripts were read into R using the "rjson" package (Couture-Beil, 2018) and subjected to further filtering. Cracks smaller than 0.5 mm^2 were treated as noise and were therefore not included in any further analysis. Filtered image data were then assembled into data tables and merged with image acquisition times that were obtained from. EXIF tags of original images using the R-package "exiftoolr" (O'Brien, 2019). For further analysis, hourly average values were computed for every
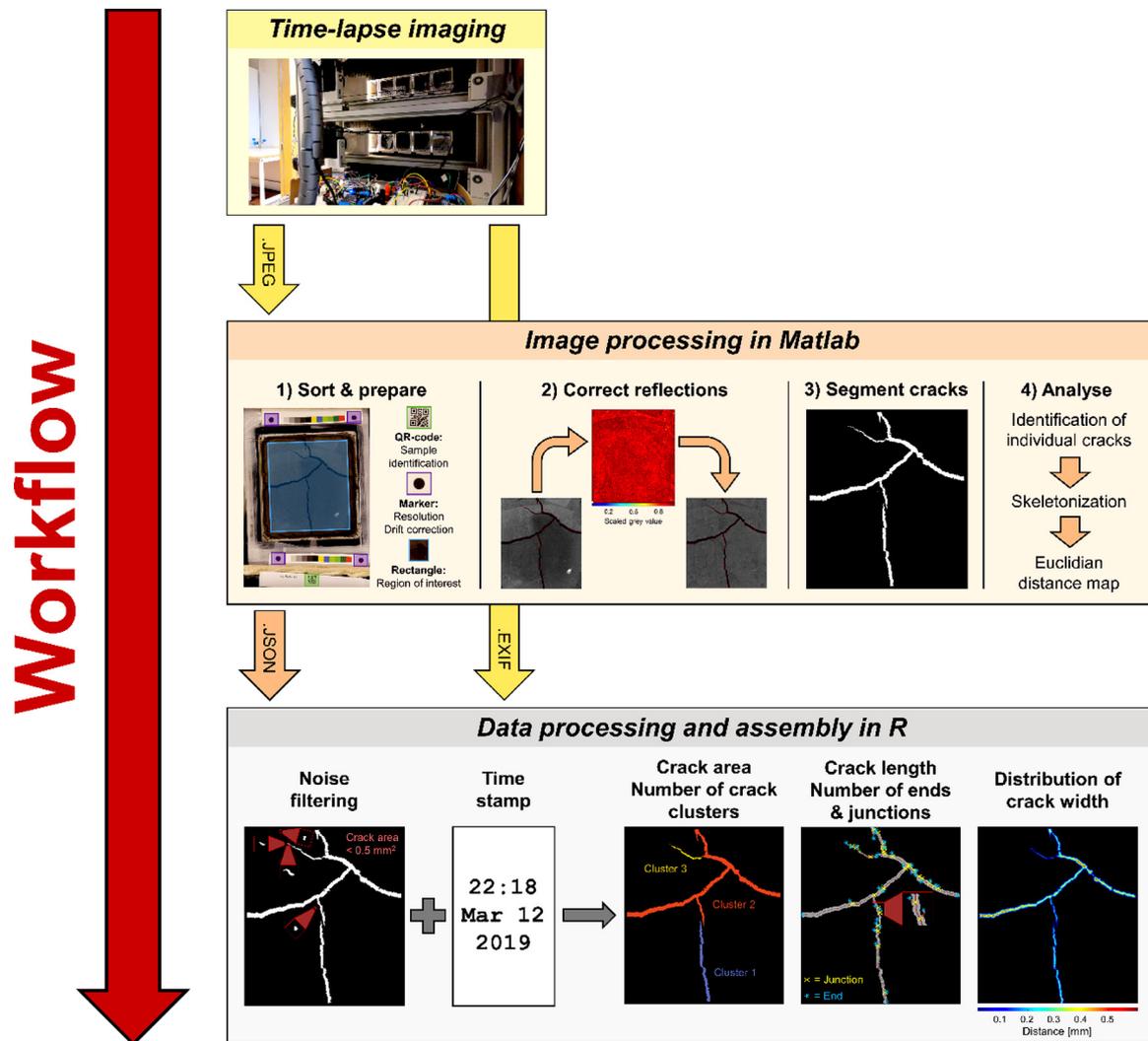
Fig. 3. Schematic illustration of the workflow in the platform: Images were acquired with the set-up shown in Fig. 2 and stored as. JPEG. Image analysis was done in a series of Matlab scripts that 1) identified and sorted images, determined pixel resolution and corrected for horizontal drift between images, and defined region of interest, 2) corrected grey values for reflections from the illumination system, 3) segmented cracks and 4) extracted properties of segmented cracks, which were stored as. JSON files. Post-processing of data derived from Matlab scripts was done in R. Cracks below a size threshold (area < 0.5 mm^2) were removed, crack properties were merged with time stamps obtained from. EXIF tags of original. JPEG images and assembled into data tables.

parameter describing the crack network (Fig. 3).

Effects of drying intensity, soil type, and their interaction on crack network properties were evaluated after 0.5, 1.5, 2.5, 3.5, 4.5, 5.5 and 6.5 days of soil drying using analysis of variance. Furthermore, analysis of variance was applied to test the effects of drying intensity, soil type, and their interaction on gravimetric water content and soil shrinkage after 6.5 days of soil drying. Shapiro-Wilk tests and visual assessments of residual plots were used to check for normality of residual distributions. Data were log-transformed if the assumption of normality was violated. Treatment means were compared with Tukey's honest significant difference tests at p < 0.05 as implemented in the R-package "agricolae" (de Mendiburu, 2017d).

3. Results

3.1. Temporal development of crack network

The extent of the crack network, assessed by total crack length and mean crack width, increased over time for all drying intensities and soils (Fig. 4). Except for the clay soil at high drying intensity, the temporal development of crack length and mean crack width were well synchronized. Total crack length and mean crack width increased at a

high rate during the first 24–48 h of soil drying. After that, both parameters continued to increase at a much slower rate (Fig. 4). In the treatment with clay soil and high drying intensity, we observed a shift in the temporal development of total crack length and mean crack width. The increase in crack length started to slow down remarkably after 24 h of soil drying, whereas mean crack width kept increasing at a relatively high rate for another 24–48 h before slowing down (Fig. 4). This indicates that in response to high drying intensity, cracks in the clay soil kept widening up substantially after initial crack opening. In the other treatments, a widening of cracks after primary crack occurrence was much less pronounced. Total crack area and maximum crack width showed similar temporal dynamics as crack length and mean crack width (Supplemental Figure Fig S2). Although we excluded cracks close to the wall of the soil box (Fig. 3), it is possible that edge effects influenced the spatial extent of the crack system.

The complexity of the crack network also increased with time. In the clay and clay loam soil, the increase in the number of crack endpoints was higher in the first 24–48 h of drying than in the remaining time (Fig. 5). In the silt loam soil, this pattern was even more pronounced. After an increase in the number of crack endpoints for around 24 h, there was hardly any increase visible anymore. Moreover, under moderate drying intensity, the number of crack endpoints in the silt loam
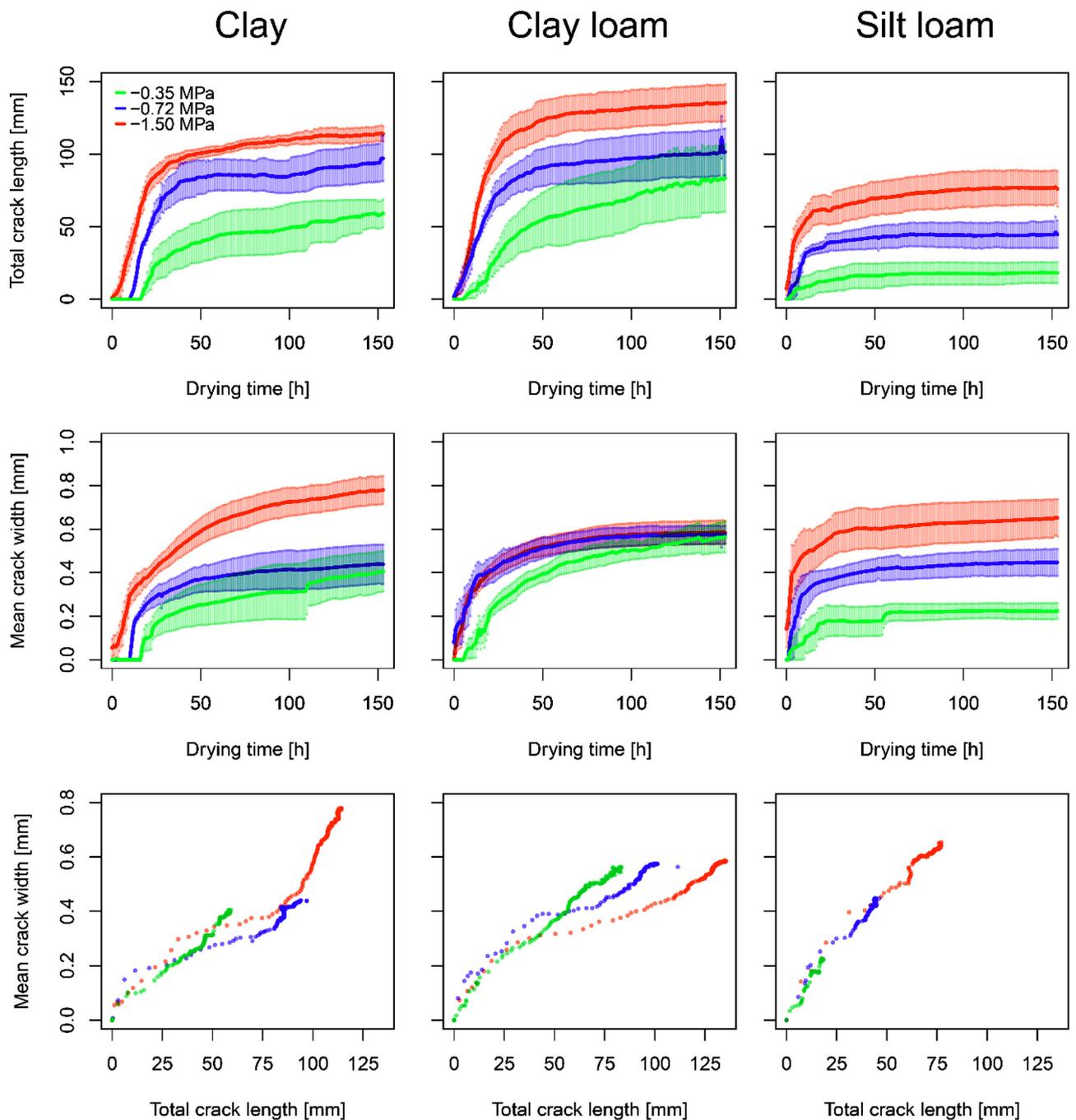
Fig. 4. Temporal development of (top) total crack length and (middle) mean crack width due to localized soil drying at three drying intensities in three soils, and (bottom) relationship between total crack length and mean crack width. Colours indicate the osmotic potential of the polyethylene glycol solution used for the different drying intensities (green = -0.35 MPa, low; blue = -0.72 MPa, moderate; red = -1.50 MPa, high). Line and circles represent mean values, and shaded area represents standard error (n = 4).

soil even slightly decreased from 48 h until the end of the experiment (Fig. 5). The number of crack junctions, another metric to quantify the complexity of the crack network, followed a similar temporal pattern as the number of crack endpoints (Supplemental Figure S3). Finally, the number of crack clusters also changed over time. Particularly under high drying intensity, the number of crack clusters increased for about 24–48 h before it started to decrease again (Fig. 5). This indicates that the crack network started with the formation of individual cracks, which later connected to each other. Hence, the connectivity of the crack network was low at first but increased with time. We observed similar but less pronounced patterns at moderate drying intensity, while at low drying intensity the number of crack clusters stabilized

after 24–48 h of soil drying (Fig. 5).

3.2. Effects of drying intensity and soil type on crack network properties

Crack networks differed between soil types and drying intensities. In general, higher drying intensity and higher clay content resulted in larger and more complex crack networks (Fig. 6). Most of the assessed properties describing the extent, complexity, and the connectivity of crack networks were significantly affected by drying intensity and soil type (Table 3, Supplemental Table S1).

The extent of the crack network was significantly affected by drying intensity at all time points, i.e. after 0.5, 1.5, 2.5, 3.5, 4.5, 5.5 and 6.5
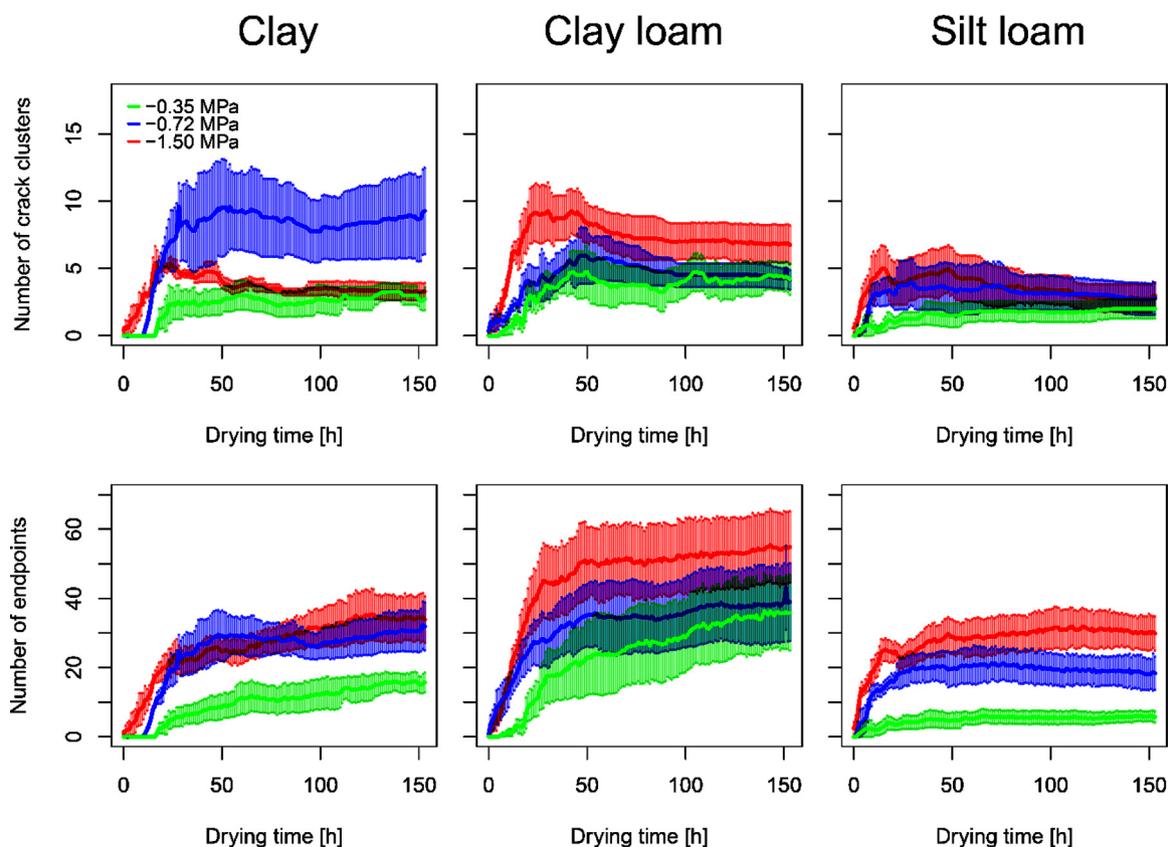
Fig. 5. Temporal development of (top) number of isolated crack clusters and (bottom) number of crack endpoints due to localized soil drying at three drying intensities in three soils. Colours indicate the osmotic potential of the polyethylene glycol solution used for the different drying intensities (green = -0.35 MPa, low; blue = -0.72 MPa, moderate; red = -1.50 MPa, high). Line and shaded area represent mean values and standard errors, respectively (n = 4).

days of soil drying. Significant effects of drying intensity ($p < 0.001$) occurred for total crack length and mean crack width (Table 3), as well as total crack area and maximum crack width (Supplemental Table S1). Across soil types, total crack length and mean crack width increased with drying intensity (Fig. 4). Similar effects of drying intensity occurred for total crack area and maximum crack width (Supplemental Figure S2). Furthermore, drying intensity significantly affected the complexity of the crack network at all time points. The number of crack endpoints (Table 3) and the number of crack junctions (Supplemental Table S1) showed significant responses to drying intensity. In all soil types, the crack network was more complex under higher drying intensity as reflected by greater number of crack endpoints (Fig. 5) and crack junctions (Supplemental Figure S3). Moreover, significant effects of drying intensity on the number of crack clusters occurred at the beginning of the drying period (Table 3). A lower number of crack clusters, indicating better crack connectivity was observed under lower drying intensity. However, in the clay soil the highest number of crack clusters and thus the lowest connectivity was found under moderate drying intensity (Fig. 5).

Most crack system properties differed between soil types. Total crack length (Table 3), total crack area, and maximum crack width (Supplemental Table S1) showed significant responses to soil type at all time points. Crack length (Fig. 4), crack area, and maximum crack width (Supplemental Figure S2) were smaller in the silt loam soil than in the clay and clay loam soil. Significant effects of soil type on mean crack width were limited to the first time point, corresponding to 0.5 days of soil drying ($p < 0.01$; Table 3). The complexity of the crack system was also significantly affected by soil type. The number of crack endpoints (Table 3) and the number of crack junctions (Supplemental Table S1) showed significant response to soil type at all seven time points. The highest crack network complexity was found in the clay

loam soil, followed by the clay soil and the silt loam soil (Fig. 5, Supplemental Figure S3). Significant effects of soil type on the number of crack clusters occurred after 0.5, 4.5, 5.5 and 6.5 days of soil drying (Table 3). The number of crack clusters tended to be the lowest in the silt loam soil (Fig. 5). With a few exceptions, no significant effects of the interaction between drying intensity and soil type on crack network properties were observed (Table 3, Supplemental Table S1).

3.3. Effects of drying intensity and soil type on soil shrinkage and final soil water content

Across all treatments, gravimetric soil water content decreased from $0.30 - 0.31$ g g^{-1} at the start of the experiment (Table 1) to $0.10 - 0.19$ g g^{-1} at the end of the experiment. Hence, soil water content deceased by 40–67 % due to soil drying for 6.5 days (Fig. 7). Moreover, soil water content at the end of the experiment was significantly affected by drying intensity ($p < 0.001$) and soil type ($p < 0.05$). Soil water content decreased in response to higher drying intensity in all three soils (Fig. 7). Four samples were connected to the same reservoir of PEG solution and the cumulative water loss of four samples was between 8.7 and 15.1 mL. This caused a dilution of the PEG solution of approximately 1–1.5 %. The resulting reduction of the osmotic potential from the start until the end of a drying experiment was less than 5% (Supplemental Figure S4). The flow rate of PEG solution in the system was 1.44 L h^{-1} and thus several orders of magnitudes higher than the drying rate of the soil samples. Therefore, dilution of the PEG solution between connected samples was negligible.

Soil shrinkage at the end of the experiment was between 0.3 % and 5.1 % (Fig. 7). The latter number corresponds to a maximum increase in the average density of the soil matrix from 1.3 g cm^{-3} at the beginning of the experiment (Table 1) to 1.36 g cm^{-3} after 6.5 days. In line with
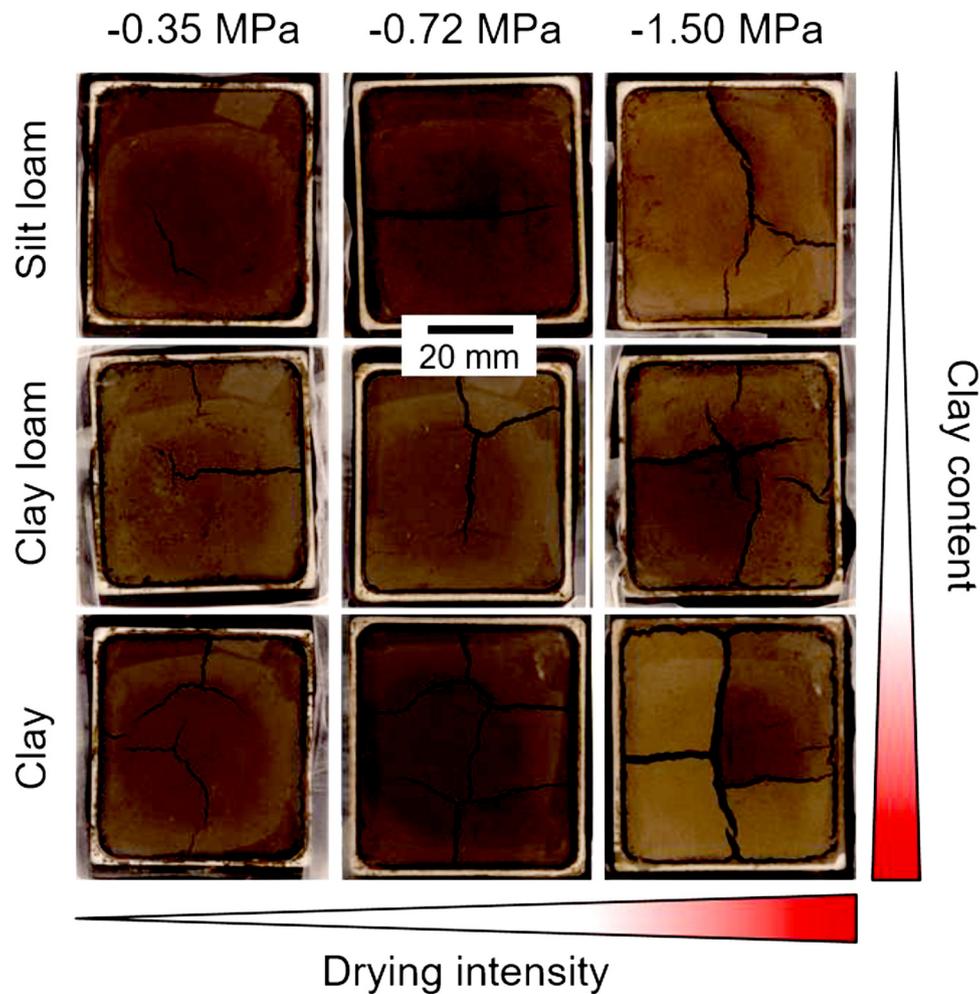
Fig. 6. Typical examples of crack networks after 6.5 days of localized soil drying. The osmotic potential of the polyethylene glycol solution used for different drying intensities increases from left to right and the clay content increases from top to bottom.

responses of soil water content, soil shrinkage was significantly affected by drying intensity (p < 0.001) and soil type (p < 0.001). Shrinkage increased with drying intensity in all three soils. Differences between soil types were particularly pronounced at high drying intensity, where soil shrinkage was significantly lower (Tukey HSD test, p < 0.05) in the silt loam soil than in the clay soil (Fig. 7).

4. Discussion

In this study, we present a platform to quantify spatiotemporal dynamics of soil crack networks due to simulated root water uptake. Polyethylene glycol solution was pumped through dialysis tubes, which induced localized soil drying at the contact area between the soil and the dialysis tube (Cui and Delage, 1996; Delage and Cui, 2008). Changing the concentration and thus the osmotic potential of the PEG

Table 3
Summary statistics on the effects of drying intensity (DI), soil type (ST), and their interaction (DI:ST) on properties of the soil crack network after different times of localized soil drying obtained from analysis of variance. ***, **, * denote significant effects at p < 0.001, 0.01 and 0.05, respectively, ns denotes non-significant effects (n = 4).

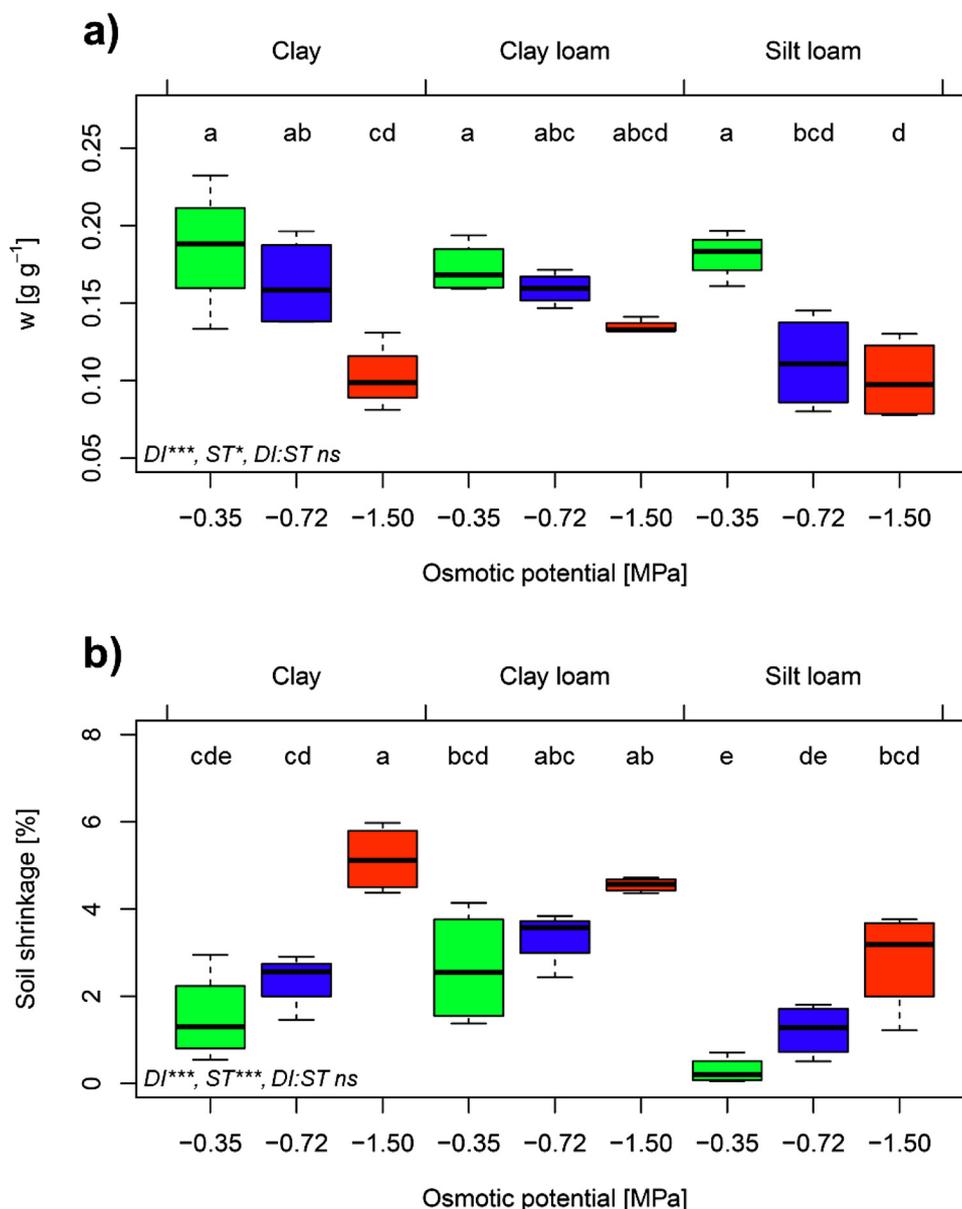|			Drying time [d]						
Crack system property	Transformation	Effect	0.5	1.5	2.5	3.5	4.5	5.5	6.5
Total crack length [mm]		DI	***	***	***	***	***	***	***
		ST	**	***	***	***	***	***	***
		ST:DI	ns	ns	ns	ns	ns	ns	ns
Mean crack width [mm]		DI	***	***	***	***	***	***	***
		ST	**	ns	ns	ns	ns	ns	ns
		ST:DI	ns	ns	ns	ns	ns	*	*
Number of crack clusters [#]	$\log_{10}$	DI	***	**	ns	*	ns	ns	ns
		ST	**	ns	ns	ns	*	*	*
		ST:DI	ns	ns	ns	ns	ns	ns	ns
Number of crack endpoints [#]		DI	***	***	**	**	**	**	**
		ST	***	**	*	**	**	**	**
		ST:DI	ns	ns	ns	ns	ns	ns	ns

Fig. 7. Influence of osmotic potential of polyethylene glycol solution used for different drying intensities (DI), and soil type (ST) on a) gravimetric water content after 6.5 days of drying and b) shrinkage of the soil matrix. *** and * denote significant effects of DI, ST and their interaction (DI:ST) at p < 0.001 and 0.05, respectively, ns denotes non-significant effects, obtained from analysis of variance. Different letters indicate significant differences using Tukey's honest significance difference test at p < 0.05 (n = 4).

solution, allowed us to dry the soil at different yet controlled intensities, which is challenging when working with living plants (Zarebanadkouki et al., 2014, 2013). We quantified crack networks that developed in response to localized soil drying with a time-lapse imaging system and a newly developed image analysis pipeline.

4.1. Time-lapse imaging allows quantification of crack network development at high temporal resolution

Automated time-lapse imaging (Fig. 2) and subsequent image processing (Fig. 3) allowed quantifying spatiotemporal dynamics of the crack network in response to simulated root water uptake. We assessed the temporal development of crack networks with a set of parameters describing the extent, the complexity, and the connectivity of the crack network. Due to soil shrinkage, gaps between the soil and the walls of the soil boxes occurred. Similar effects have been observed in previous studies investigating soil structure dynamics at the column scale (Pires

et al., 2020; Sandin et al., 2018). Therefore, we had to exclude sample edges from image analysis (Fig. 3), which most likely resulted in an underestimation of soil matrix shrinkage (Fig. 7). However, since the presented set-up is not tied to a given size of the sample, edge effects on soil shrinkage could be reduced or completely avoided by increasing the box size. Similarly, the use of larger soil boxes could reduce potential edge effects on crack network development.

In line with previous studies (Decarlo and Shokri, 2014; Tran et al., 2019), the most pronounced changes in the crack network happened during the first 24–48 hours of soil drying (Figs. 4 and 5, Supplemental Figures S2 and S3). Time-lapse imaging as deployed here and elsewhere (Decarlo and Shokri, 2014; Tran et al., 2019; Zhang et al., 2020; Zhu et al., 2020) limits observations to two dimensions but offers the opportunity for quantification at high temporal resolution. Due to time-consuming image acquisition and analysis, the temporal resolution of techniques allowing for quantification in three dimensions such as X-ray tomography is limited (Diel et al., 2019; Pires et al., 2020; Sandin

et al., 2018). The fast development of soil cracks in response to drying observed here and in other studies (Decarlo and Shokri, 2014; Tran et al., 2019) highlights the need for methods that enable for quantifications at high temporal resolution. Moreover, water uptake in plants happens within hours (Tötzke et al., 2017; Zarebanadkouki et al., 2014, 2013), which further demonstrates the need for high temporal resolutions. Our platform allows for quantifications at temporal resolutions that match the temporal scale of root water uptake and soil crack formation.

4.2. Soil type and drying intensity influence crack network development

We observed significant effects of the soil type on different parameters describing the crack network (Table 3). In accordance with previous studies quantifying soil structure dynamics in response to evaporative drying (Diel et al., 2019; Materechera et al., 1992; Sandin et al., 2018; Zhang et al., 2016), the extent (Fig. 4, Supplemental Figure S2) and the complexity of the crack network (Fig. 5, Supplemental Figure S3) was higher in the clay and clay loam soil than in the silt loam soil. The temporal development of different parameters describing the extent of the crack network was well synchronized across treatments, except for the clay soil that was dried at high intensity. In this treatment, cracks considerably widened after primary crack occurrence as indicated by the temporal shift in the development of crack length and crack width (Fig. 4). As observed by Decarlo and Shokri (2014) under evaporative soil drying, crack connectivity under moderate and high drying intensity increased with time as indicated by the decreasing number of crack clusters (Fig. 5). A higher number of crack clusters coincided with an increased extent and complexity of the crack network (Figs. 4 and 5, Supplemental Figures S2 and S3). Hence, larger and more complex crack networks were less connected than smaller and less complex networks. These effects of drying intensity on crack network development are in line with previous results showing that differences in water uptake among plant species affect the porosity of soil aggregates (Materechera et al., 1992). Our results and previous studies (Diel et al., 2019; Materechera et al., 1992; Sandin et al., 2018; Zhang et al., 2016) clearly demonstrate that soil structure dynamics are influenced by drying intensity and soil properties such as texture (Fig. 6). Methods that allow for high sample throughput are needed to account for this variability. Mostly due to high equipment costs, the throughput that is possible with X-ray or neutron tomography remains limited. Our platform provides an opportunity to overcome these limitations. Simultaneous RGB time-lapse imaging of twelve specimens enabled to achieve a relatively high throughput at low costs.

4.3. Potential of the platform in future studies

In the current study, we tested the developed platform with three soil types and three drying intensities. Since the platform allows for high sample throughput, it is possible to test a larger number of soils and drying intensities. Our platform also offers the possibility to investigate effects of root exudation on the development of crack networks. Root exudates such as organic acids could be added to the soil through retrodialysis using microanalysis probes that are inserted into the soil sample (Buckley et al., 2020; McKay Fletcher et al., 2019). We recorded crack network development due to simulated water uptake during one drying cycle. However, soil is regularly rewetted under field conditions, which leads to crack closing (Diel et al., 2019). To account for this, future studies could quantify the dynamics of cracks networks during multiple drying-rewetting cycles. Moreover, the combination of RGB and hyperspectral imaging (Fabre et al., 2015; Weidong et al., 2003) would enable to relate crack formation and closing to spatial information on soil moisture dynamics. Particle image velocimetry and data on crack tip opening angle obtained from time-lapse image series have been applied to describe the mechanics underlying crack formation in soil (Azmatch et al., 2008; Hallett and Newson, 2005; Yoshida

and Hallett, 2008). The high temporal resolution possible with our platform offers the opportunity to use such approaches to identify mechanisms that govern crack network development induced by root water uptake. To better represent real soil-plant interactions, sieved soil could be replaced by less disturbed samples, and the artificial roots used here could be replaced by living plants. Another option to better represent plant roots would be to use thinner dialysis tubes. Eventually, linkages between root water uptake, soil crack formation and aboveground plant physiological processes need to be investigated to better understand how plants contribute to soil structure dynamics and soil functioning.

5. Conclusion

We developed a time-lapse imaging platform to quantify spatiotemporal dynamics of soil crack networks in response to localized soil drying. Polyethylene glycol solution with different osmotic potentials was used to induce soil drying, thereby simulating root water uptake at different intensities. Automated time-lapse imaging was applied to record crack network development at high temporal resolution, and an image analysis pipeline was developed to quantify properties of the crack network. Experiments with three soils that were subjected to three drying intensities demonstrated that the platform is suitable to quantify spatiotemporal crack development in response to soil drying under a wide range of conditions. Significant effects of soil type and drying intensity on the extent, the complexity and the connectivity of the crack network were observed. Hence, we demonstrate that the platform can provide new insights into interactions between root water uptake and soil crack formation.

Declaration of Competing Interest

The authors declare that they have no known competing financial interests or personal relationships that could have appeared to influence the work reported in this paper.

Appendix A. Supplementary data

Supplementary material related to this article can be found, in the online version, at doi:https://doi.org/10.1016/j.still.2020.104769.

References

Angers, D.A., Caron, J., 1998. Plant-induced changes in soil structure: processes and feedbacks. Biogeochemistry 42, 55–72. https://doi.org/10.1023/A:1005944025343.

Atkinson, J.A., Hawkesford, M.J., Whalley, W.R., Zhou, H., Mooney, S.J., 2020. Soil strength influences wheat root interactions with soil macropores. Plant Cell Environ. 43, 235–245. https://doi.org/10.1111/pce.13659.

Azmatch, T.F., Arenson, L.U., Sego, D.C., Biggar, K.W., 2008. Measuring ice Lens growth and development of soil strains during frost penetration using particle image velocimetry (GeoPIV) image analysis using GeoPIV ice Lens growth and deformation. 9th Int. Conf. Permafr. 89–93.

Bronick, C.J.J., Lal, R., 2005. Soil structure and management: a review. Geoderma 124, 3–22. https://doi.org/10.1016/j.geoderma.2004.03.005.

Buckley, S., Brackin, R., Jämtgård, S., Näsholm, T., Schmidt, S., 2020. Microdialysis in soil environments: current practice and future perspectives. Soil Biol. Biochem. 143.

https://doi.org/10.1016/j.soilbio.2020.107743.

Capowiez, Y., Samartino, S., Cadoux, S., Bouchant, P., Richard, G., Boizard, H., 2012. Role of earthworms in regenerating soil structure after compaction in reduced tillage systems. Soil Biol. Biochem. 55, 93–103. https://doi.org/10.1016/j.soilbio.2012.06.013.

Cheik, S., Bottinelli, N., Minh, T.T., Doan, T.T., Jouquet, P., 2019. Quantification of three dimensional characteristics of macrofauna macropores and their effects on soil hydraulic conductivity in northern Vietnam. Front. Environ. Sci. 7, 1–10. https://doi.org/10.3389/fenvs.2019.00031.

Colombi, T., Keller, T., 2019. Developing strategies to recover crop productivity after soil compaction—A plant eco-physiological perspective. Soil Tillage Res. 191, 156–161. https://doi.org/10.1016/j.still.2019.04.008.

Colombi, T., Braun, S., Keller, T., Walter, A., 2017. Artificial macropores attract crop roots and enhance plant productivity on compacted soils. Sci. Total Environ. 574, 1283–1293. https://doi.org/10.1016/j.scitotenv.2016.07.194.

Couture-Beil, A., 2018. Rjson: JSON for R.Rjson: JSON for R.

Crombie, D.S., Tippett, J.T., Hill, T.C., 1988. Dawn water potential and root depth of trees and understorey species in South-western Australia. Aust. J. Bot. 36, 621–631. https://doi.org/10.1071/BT9880621.

Cui, Y.J., Delage, P., 1996. Yielding and plastic behaviour of an unsaturated compacted silt. Géotechnique 46, 291–311. https://doi.org/10.1680/geot.1996.46.2.291.

de Mendiburu, F., 2017d. Agricolae: Statistical Procedures for Agricultural Research.Agricolae: Statistical Procedures for Agricultural Research.

Decarlo, K.F., Shokri, N., 2014. Effects of substrate on cracking patterns and dynamics in desiccating clay layers. Water Resour. Res. 50, 3039–3051. https://doi.org/10.1002/2013WR014466.

Delage, P., Cui, Y.J., 2008. An evaluation of the osmotic method of controlling suction. Geomech. Geoengin. 3, 1–11. https://doi.org/10.1080/17486020701868379.

Dexter, A.R., 1991. Amelioration of soil by natural processes. Soil Tillage Res. 20, 87–100.

Diel, J., Vogel, H.J., Schlüter, S., 2019. Impact of wetting and drying cycles on soil structure dynamics. Geoderma 345, 63–71. https://doi.org/10.1016/j.geoderma.2019.03.018.

Fabre, S., Briottet, X., Lesaignoux, A., 2015. Estimation of soil moisture content from the spectral reflectance of bare soils in the 0.4–2.5 µm domain. Sensors (Switzerland) 15, 3262–3281. https://doi.org/10.3390/s150203262.

Fiscus, E.L., 1972. In situ measurement of root-water potential. Plant Physiol. 50, 191–193.

Ghezzehei, T.A., 2012. Soil structure. In: Huang, P.M., Li, Y., M.E.S (Eds.), Handbook of Soil Sciences: Vol. 1 Properties and Processes. CRC Press, Boca Raton, pp. 1–17. https://doi.org/10.1080/03670074.1944.11664380.

Hallett, P.D., Newson, T.A., 2005. Describing soil crack formation using elastic-plastic fracture mechanics. Eur. J. Soil Sci. 56, 31–38. https://doi.org/10.1111/j.1365-2389.2004.00652.x.

Hallett, P.D., Karim, K.H., Bengough, Glyna., Otten, W., 2013. Biophysics of the vadose zone: from reality to model systems and Back again. Vadose Zo. J. 12. https://doi.org/10.2136/vzj2013.05.0090.

Hamza, Ma., Anderson, W.K.K., 2005. Soil compaction in cropping systems. Soil Tillage Res. 82, 121–145. https://doi.org/10.1016/j.still.2004.08.009.

Harvey, P., 2018. Exiftool 10.61.

Jarvis, N.J., 2007. A review of non-equilibrium water flow and solute transport in soil macropores: principles, controlling factors and consequences for water quality. Eur. J. Soil Sci. 58, 523–546. https://doi.org/10.1111/j.1365-2389.2007.00915.x.

Jin, K., Shen, J., Ashton, R.W., Dodd, I.C., Parry, M.A.J., Whalley, W.R., 2013. How do roots elongate in a structured soil? J. Exp. Bot. 64, 4761–4777. https://doi.org/10.1093/jxb/ert286.

Kautz, T., Lüsebrink, M., Pätzold, S., Vetterlein, D., Pude, R., Athmann, M., Küpper, P.M., Perkons, U., Köpke, U., 2014. Contribution of anecic earthworms to biopore formation during cultivation of perennial ley crops. Pedobiologia (Jena). 57, 47–52. https://doi.org/10.1016/j.pedobi.2013.09.008.

Koestel, J., Schlüter, S., 2019. Quantification of the structure evolution in a garden soil over the course of two years. Geoderma 338, 597–609. https://doi.org/10.1016/j.geoderma.2018.12.030.

Kroon, D.-J., 2009. Region Growing. MATLAB Central File Exchange.Region Growing. MATLAB Central File Exchange.

Lavelle, P., Bignell, D., Lepage, M., Wolters, V., Roger, P., Ineson, P., Heal, O.W., Dhillion, S., 1997. Soil function in a changing world: the role of invertebrate ecosystem engineers. Eur. J. Soil Biol. 33, 159–193.

Lucas, M., Schlüter, S., Vogel, H.J., Vetterlein, D., 2019a. Soil structure formation along an agricultural chronosequence. Geoderma 350, 61–72. https://doi.org/10.1016/j.geoderma.2019.04.041.

Lucas, M., Schlüter, S., Vogel, H.J., Vetterlein, D., 2019b. Roots compact the surrounding soil depending on the structures they encounter. Sci. Rep. 9, 1–13. https://doi.org/10.1038/s41598-019-52665-w.

Materechera, S.A., Dexter, A.R., Alston, A.M., 1992. Formation of aggregates by plant roots in homogenised soils. Plant Soil 142, 69–79. https://doi.org/10.1007/BF00010176.

Mawodza, T., Burca, G., Casson, S., Menon, M., 2020. Wheat root system architecture and soil moisture distribution in an aggregated soil using neutron computed tomography. Geoderma 359, 113988. https://doi.org/10.1016/j.geoderma.2019.113988.

McKay Fletcher, D.M., Shaw, R., Sánchez-Rodríguez, A.R., Daly, K.R., van Veelen, A., Jones, D.L., Roose, T., 2019. Quantifying citrate-enhanced phosphate root uptake using microdialysis. Plant Soil. https://doi.org/10.1007/s11104-019-04376-4.

Money, N.P., 1989. Osmotic pressure of aqueous polyethylene glycols - relationship between molecular weight and vapor pressure deficit. Plant Physiol. 91, 766–769. https://doi.org/10.1104/pp.91.2.766.

O'Brien, J., 2019. Exiftoolr: ExifTool Functionality from R.Exiftoolr: ExifTool Functionality from R.

Oades, J.M., 1993. The role of biology in the formation, stabilization and degradation of soil structure. Geoderma 56, 377–400. https://doi.org/10.1016/0016-7061(93)90123-3.

Pires, L.F., Auler, A.C., Roque, W.L., Mooney, S.J., 2020. X-ray microtomography analysis of soil pore structure dynamics under wetting and drying cycles. Geoderma 362, 114103. https://doi.org/10.1016/j.geoderma.2019.114103.

Pulido-Moncada, M., Katuwal, S., Ren, L., Cornelis, W., Munkholm, L., 2020. Impact of potential bio-subsoilers on pore network of a severely compacted subsoil. Geoderma 363, 114154. https://doi.org/10.1016/j.geoderma.2019.114154.

R Core Team, 2017. R: A Language and Environment for Statistical Computing.R: A Language and Environment for Statistical Computing.

Rabot, E., Wiesmeier, M., Schlüter, S., Vogel, H.J., 2018. Soil structure as an indicator of soil functions: a review. Geoderma 314, 122–137. https://doi.org/10.1016/j.geoderma.2017.11.009.

Sandin, M., Jarvis, N., Larsbo, M., 2018. Consolidation and surface sealing of nine harrowed Swedish soils. Soil Tillage Res. 181, 82–92. https://doi.org/10.1016/j.still.2018.03.017.

Shapira, L., 2015. QR code encode and decode. MATLAB Central File Exchange.

Sharp, R.E., Davies, W.J., 1979. Solute regulation and growth by roots and shoots of water-stressed maize plants. Planta 147, 43–49. https://doi.org/10.1007/BF00384589.

Simonneau, T., Barrieu, P., Tardieu, F., 1998. Accumulation rate of ABA in detached maize roots correlates with root water potential regardless of age and branching order. Plant, Cell Environ. 21, 1113–1122. https://doi.org/10.1046/j.1365-3040.1998.00344.x.

Solís Montero, A., Lang, J., 2012. Skeleton pruning by contour approximation and the integer medial axis transform. Comput. Graph. 36, 477–487. https://doi.org/10.1016/j.cag.2012.03.029.

Stirzaker, R.J.J., Passioura, J.B.B., Wilms, Y., 1996. Soil structure and plant growth: impact of bulk density and biopores. Plant Soil 185, 151–162. https://doi.org/10.1007/BF02257571.

Tötzke, C., Kardjilov, N., Manke, I., Oswald, S.E., 2017. Capturing 3D Water flow in rooted soil by ultra-fast neutron tomography. Sci. Rep. 7, 1–9. https://doi.org/10.1038/s41598-017-06046-w.

Tracy, S.R., Black, C.R., Roberts, J.A., Mooney, S.J., 2011. Soil compaction: a review of past and present techniques for investigating effects on root growth. J. Sci. Food Agric. 91, 1528–1537. https://doi.org/10.1002/jsfa.4424.

Tracy, S.R., Black, C.R., Roberts, J.A., McNeill, A., Davidson, R., Tester, M., Samec, M., Korošak, D., Sturrock, C., Mooney, S.J., 2012. Quantifying the effect of soil compaction on three varieties of wheat (triticum aestivum L.) Using X-ray micro computed tomography (CT). Plant Soil 353, 195–208. https://doi.org/10.1007/s11104-011-1022-5.

Tran, D.K., Ralaizafisoloarivony, N., Charlier, R., Mercatoris, B., Léonard, A., Toye, D., Degré, A., 2019. Studying the effect of desiccation cracking on the evaporation process of a luvisol – from a small-scale experimental and numerical approach. Soil Tillage Res. 193, 142–152. https://doi.org/10.1016/j.still.2019.05.018.

United States Department of Agriculture, 2020. Soil Texture Calculator [WWW Document]. Nat. Resour. Conserv. Serv. - Soils. URL https://www.nrcs.usda.gov/wps/portal/nrcs/detail/soils/survey/?cid=nrcs142p2_054167 (accessed 1.30.20).

Vogel, H.J., Bartke, S., Daedlow, K., Helming, K., Kögel-Knabner, I., Lang, B., Rabot, E., Russell, D., Stößel, B., Weller, U., Wiesmeier, M., Wollschläger, U., 2018. A systemic approach for modeling soil functions. Soil 4, 83–92. https://doi.org/10.5194/soil-4-83-2018.

Weidong, L., Baret, F., Xingfa, G., Bing, Z., Qingxi, T., Lanfen, Z., 2003. Evaluation of methods for soil surface moisture estimation from reflectance data. Int. J. Remote Sens. 24, 2069–2083. https://doi.org/10.1080/01431160210163155.

Williams, J., 1976. Dependence of root Water potential on root radius and density. J. Exp. Bot. 27, 121–124.

Yoshida, S., Hallett, P.D., 2008. Impact of hydraulic suction history on crack growth mechanics in soil. Water Resour. Res. 44, 1–9. https://doi.org/10.1029/2007WR006055.

Young, I.M., Blanchart, E., Chenu, C., Dangerfield, M., Fragoso, C., Grimaldi, M., Ingram, J., Monrozier, L.J., 1998. The interaction of soil biota and soil structure under global change. Glob. Chang. Biol. 4, 703–712. https://doi.org/10.1046/j.1365-2486.1998.00194.x.

Zarebanadkouki, M., Kim, Y.X., Carminati, A., 2013. Where do roots take up water? Neutron radiography of water flow into the roots of transpiring plants growing in soil. New Phytol. 199, 1034–1044. https://doi.org/10.1111/nph.12330.

Zarebanadkouki, M., Kroener, E., Kaestner, A., Carminati, A., 2014. Visualization of root water uptake: quantification of deuterated water transport in roots using neutron radiography and numerical modeling. Plant Physiol. 166, 487–499. https://doi.org/10.1104/pp.114.243212.

Zhang, Z.B., Zhou, H., Zhao, Q.G., Lin, H., Peng, X., 2014. Characteristics of cracks in two paddy soils and their impacts on preferential flow. Geoderma 228–229, 114–121. https://doi.org/10.1016/j.geoderma.2013.07.026.

Zhang, Z.B., Zhou, H., Lin, H., Peng, X., 2016. Puddling intensity, sesquioxides, and soil organic carbon impacts on crack patterns of two paddy soils. Geoderma 262, 155–164. https://doi.org/10.1016/j.geoderma.2015.08.030.

Zhang, Y., Gu, K., Li, J., Tang, C., Shen, Z., Shi, B., 2020. Effect of biochar on desiccation cracking characteristics of clayey soils. Geoderma 364, 114182. https://doi.org/10.1016/j.geoderma.2020.114182.

Zhu, L., Shen, T., Ma, R., Fan, D., Zhang, Y., Zha, Y., 2020. Development of cracks in soil: an improved physical model. Geoderma 366, 114258. https://doi.org/10.1016/j.geoderma.2020.114258.

Zwieniecki, M.A., Boersma, L., 1997. A technique to measure root tip hydraulic conductivity and root water potential simultaneously. J. Exp. Bot. 48, 333–336. https://doi.org/10.1093/jxb/48.2.333.